PCCP

PAPER

View Article Online
View Journal | View Issue

Cite this: *Phys. Chem. Chem. Phys.*, 2015, **17**, 28060

Received 22nd December 2014,
Accepted 18th February 2015

DOI: 10.1039/c4cp06012a

www.rsc.org/pccp

Gold–palladium core@shell nanoalloys: experiments and simulations†

A. Spitale,[a] M. A. Perez,[b] S. Mejía-Rosales,[c] M. J. Yacamán[d] and M. M. Mariscal*[a]

In this work, we report a facile synthesis route, structural characterization, and full atomistic simulations of gold–palladium nanoalloys. Through aberration corrected-STEM, UV-vis spectroscopy and EDS chemical analysis, we were able to determine that Au(core)–Pd(shell) bimetallic nanoparticles were formed. Using different computational approaches, we were capable of establishing how the size of the core and the thickness of the shell will affect the thermodynamic stability of several core–shell nanoalloys. Finally, grand canonical simulations using different sampling procedures were used to study the growth mechanism of Pd atoms on Au seeds of different shapes.

1. Introduction

Nowadays, it is very well known that metal clusters and nanoparticles (NPs) present exceptional optical, electrical and catalytic properties.[1,2] The case of nanoalloys is of topmost interest and they constitute an innovative type of catalyst, mainly due to the fact that their physicochemical properties can be tuned by varying the composition and atomic arrangement as well as their sizes and shapes.[3] Among various nanoalloys, the Pd–Au system is one of the most attractive systems in catalysis;[4] since alloyed and core@shell Au–Pd structures have been used as catalysts in the oxidation reaction of CO at low temperatures,[5] acetylene to ethylene conversion,[6] oxidation of alcohols to aldehydes and production of vinyl acetate monomers, selective hydrogenation of butadiene,[7] and the Ullmann reaction of aryl chlorides in water,[8] among others.[9–11] Due to the widespread diversity of applications of Au–Pd nanocatalysts, it is crucial to comprehend the structure, surface composition and growth mechanism of Au–Pd nanoalloys.

In the past decade, several groups were able to determine that the synthesis conditions are crucial to obtain nanoalloys of various sizes, chemical composition and morphological structure. Interestingly, if the reduction reactions are conducted sequentially, then quite different results are obtained, which depend on the order in which the compounds are added. For instance, segregated structures have been reported, *i.e.* Pd(core)@Au(shell),[12] Au(core)@Pd(shell),[13–15] random solid solutions,[16] and multi-layer structures.[17] Li *et al.*[18] produced Au@Pd nanoparticles by thermal decomposition of $PdCl_2$ on previously synthesized Au seeds, and Nutt *et al.*[19] deposited Pd onto Au NPs. In both cases, it was found that the plasmon resonance of Au rapidly disappeared. The observation of such a wide variety of structures makes the study of this system even more attractive from a basic perspective.

From a theoretical perspective, the energetics, structures and segregation (chemical ordering) of Pd–Au nanoalloys have been reported, using genetic algorithms[20,21] to find the lowest-energy structures. In those studies, the binding energy and the second difference in energy were used as stability criteria. Using different parameterizations of the Gupta potential, the authors found that Pd(core)@Au(shell) segregation and Pd–Au mixing generally lead to mixed Pd–Au nanoalloys. Recently, Neyman *et al.*[22] reported results of density functional theory (DFT) calculations showing that segregation of Au atoms to the NP surface is thermodynamically favorable, where the most stable sites for Au substitution are located at the edges of the Pd-NPs. Moreover, the formation of structures with Au atoms located in the core of the nanoalloys was found to be energetically unfavorable with respect to monometallic Pd and Au NPs of the same shape and size. Oviedo *et al.*[23] show, by means of the statistic thermodynamics framework, that while Au deposits on Pd cores may be thermodynamically more stable than the bulk Au material for certain NP sizes, this is not the case for Pd deposits with respect to its bulk material.

In the present work, a combination of experimental and theoretical techniques is used to study the main growth sequences of the paradigmatic Au–Pd nanocatalysts. In particular, we report an experimental synthesis route to obtain Au@Pd core–shell nanoparticles of size less than 10 nm. Imaging and chemical

[a] *INFIQC, CONICET. Departamento de Matemática y Física, Facultad de Ciencias Químicas, Universidad Nacional de Córdoba, Córdoba, X5000HUA, Argentina. E-mail: marcelo.mariscal@conicet.gov.ar*
[b] *INFIQC, CONICET. Departamento de Fisicoquímica, Facultad de Ciencias Químicas, Universidad Nacional de Córdoba, Córdoba, X5000HUA, Argentina*
[c] *Center for Innovation and Research in Engineering and Technology, and CICFIM-Facultad de Ciencias Físico-Matemáticas, Universidad Autónoma de Nuevo León, San Nicolás de los Garza, NL 66450, Mexico*
[d] *Department of Physics and Astronomy, University of Texas at San Antonio, One UTSA Circle, San Antonio, TX 78249, USA*

† Electronic supplementary information (ESI) available. See DOI: 10.1039/c4cp06012a

characterization were performed using a multi-technique approach, *i.e.* using UV-spectroscopy, aberration corrected scanning transmission electron microscopy (Cs-STEM), and Energy Dispersive X-ray spectroscopy (EDS). Subsequently, theoretical calculations, using embedded atom potentials were used to analyze the energetic stability of core–shell structures with different shell thicknesses, core sizes and shapes. Thereafter, full atomistic simulations in the grand canonical ensemble (μ,V,T) were employed to understand the growth mechanism of Pd atoms on Au seeds, in particular how the Pd atoms attach to the Au NP seeds. Finally, the atomic configurations obtained by the grand canonical Monte Carlo (gcMC) and grand canonical Langevin Dynamics (gcLD) simulations were used as input to simulate HAADF–STEM images in order to compare experimental and simulation results.

2. Experimental section

2.1 Chemicals and materials

As a precursor for the NPs, 0.25 mM tetrachloroauric(III) acid ($HAuCl_4$, Puriss p.a.) and 2.5 mM sodium tetrachloropalladate(II) (Na_2PdCl_4, Sigma Aldrich $\geq$99.99%) stock solutions were prepared and protected from sunlight. Sodium borohydride ($NaBH_4$, tetrahedron) and hydroquinone (C_6H_4-1,4-$(OH)_2$, Anedra) were used as reducing agents. Sulfuric acid (H_2SO_4, Cicarelli 95–98%) and potassium bromide (KBr, Anedra) solutions were prepared by dissolving the appropriate amount of the reagent in deionized water. All reagents were used as received.

2.2 Preparation of Au seeds and Au@Pd bimetallic NPs

Gold nanoparticles were prepared by adding a freshly prepared solution of $NaBH_4$ (2 mL, 12 mM) to an ice cold (0 °C) aqueous solution of $HAuCl_4$ (3.9 mL, 0.254 mM), H_2SO_4 (1 mL, 1 mM) and water to reach a final volume of 10 mL, followed by vigorous mixing for 5 minutes. Before characterization by UV-vis spectroscopy, the stirring was stopped and the solution was left to warm for another 5 min until it reached room temperature. The nanoparticles were stored before being used to ensure that the maturation was completed.

Pd deposition onto the Au seeds was performed by using metastable Pd(II) solutions (baths), where the homogeneous nucleation of Pd NPs is inhibited. These baths generally contain 0.1 mM Na_2PdCl_4, 0.1 mM HQ and 10 mM KBr. When gold seeds are added into these solutions, Pd(II) reduction is catalyzed and leads to palladium deposition on the surface of gold NPs, yielding Au@Pd NPs. 1 mL of Au seed solution was diluted in 8 mL of water and 1 mL of Pd(II) bath was injected later. After 5 minutes of stirring, 100 μL of 10 mM HQ were added and the solution was left for 30 minutes with no agitation. Finally, two aliquots of 5 μL of 10 mM Pd were added 30 minutes apart. The samples for STEM analysis were taken at different stages of the reaction. This procedure is not usually employed, as in general the seeds are injected into the growth bath.

2.3 Characterization

UV-visible spectra were recorded using a Shimadzu UV-1200 spectrometer, using a 1 cm quartz cell at room temperature to analyze the optical behavior of the samples.

Samples for characterization using Scanning Transmission Electron Microscopy (STEM, JEOL JEM-200ARMF, operating at 200 kV) were prepared without any purification treatment by seeding some drops of the colloidal solutions onto a grid covered with a holey carbon film. The grids were then washed in ethanol to remove any remaining molecules.

3. Model and simulation techniques

The standard ensemble to mimic crystal growth/dissolution is the grand canonical one, where the parameters fixed during the simulation are the volume of the simulation box (V), the temperature (T), and the chemical potential μ of the atoms being deposited (in this case, Pd). Thus, we have performed extensive grand canonical simulations using two different sampling algorithms (Metropolis Monte Carlo and Langevin Dynamics) to study the growth processes of Au–Pd nanoalloys.

The grand canonical Langevin dynamics (gcLD) technique was originally developed by M. M. Mariscal and co-workers[24,25] to study the metallic deposition phenomenon on crystalline planar surfaces (electrodes). Now, the method has been extended to non-planar systems, like clusters, nanowires and bimetallic nanoparticles (NPs). Langevin dynamics is a method that extends molecular dynamics to represent the effect of perturbations caused by friction and eventual collisions occurring due to the presence of a solvent (the molecules in real systems hardly are under vacuum). For doing so, it makes use of stochastic differential equations, adding two terms to Newton's second law to approximate the effects of neglected degrees of freedom. On the other hand, temperature can be controlled, approximating the canonical ensemble. Although it does not fully represent an implicit solvent (electrostatic screening and hydrophobicity), it mimics the viscosity of the medium.

The simulation cell contains two distinct regions: the NP region, and a much larger solution region. Solvent is not modeled explicitly, but it is provided as a stochastic bath. Thus, the solution part contains only metal particles that can either be of the same element as the metal atoms of the nanoparticle or different from them. As stated above, all solution particles move according to Langevin's equation:

$$\frac{d\vec{v}}{dt} = -\frac{d\vec{r}}{dt}\gamma + \vec{F}_p + \vec{F}_r$$

where γ is the friction constant, $\vec{F}_r$ represents the random force acting on each particle and $\vec{F}_p$ represents the force due to the potential interaction (EAM) between the particles and the NP, as they do not interact with each other. The friction constant γ and the random force $\vec{F}_r$ are related by the fluctuation–dissipation theorem. The Langevin dynamics was implemented according to Ermak's algorithm.[26] All atoms interact through potentials calculated using the embedded atom method (EAM)[27] and move according to Langevin's equation but with a friction coefficient that decreases as the bond order of the metal atoms increases to mimic the interaction between the NP atoms and the implicit solvent (see Fig. S1 in the ESI†). The EAM is a local environment-dependent interatomic potential, which is particularly

effective in describing metallic systems. For a pure element a, the EAM potential is composed of three functions: the pair energy Φ, the electron density ρ, and the embedding energy F. For an alloy, the EAM potential contains not only the three functions for each of the constituent elements, but also the pair energy Φ_{ab} between different elements a and b. In our code, the potentials are normalized and unified cutoff functions are used, so this energy can be constructed from elemental EAM potentials as:

$$\Phi_{ab} = \frac{1}{2}\left(\frac{f_b(r)}{f_a(r)}\Phi_{aa} + \frac{f_a(r)}{f_b(r)}\Phi_{bb}\right)$$

where $f_j(r)$ is the electron density at the site of the atom arising from atom j at a distance r and Φ_{ij} represents a two-body interaction between atoms i and j separated by r. More details can be found in Appendix A of ref. 27. The most common way of devising the embedding function and pair potentials is to fit some physically reasonable functional forms to materials properties such as lattice constant and cohesive energies. The potentials used in this work are well fitted to basic material properties such as lattice constants, elastic constants, bulk moduli, vacancy formation energies, and sublimation energies, and they predict reasonably well the heats of solution.

Grand canonical MC simulations were performed in order to compare if some concerted process can affect the growth sequence. The Metropolis Monte Carlo (MMC) algorithm[11] was used to sample the configuration space. The importance sample scheme in our gcMC procedure involves the following trial moves:

Atomic vibration: this is attempted within a small region, around the coordinate of the i atom, and the new configuration is accepted with the probability:

$$W_{j\rightarrow i} = \min[1,\exp(-\beta\Delta E_{ij})]$$

where ΔE_{ij} is the potential energy change associated with the motion of an atom calculated with the embedded atom potential. This trial move mimics the lattice vibration as well as self-diffusion processes.

Addition of an atom: an attempt is made to insert a Pd atom at a random position on the surface of the NP. The new configuration is accepted with a probability:

$$W_{N_M\rightarrow N_M+1} = \min[1,\Gamma\exp(\beta\{\mu - \Delta E_{N_M+1,N_M}\})]$$

where $\Gamma = V_{acc}/\Lambda^3(N_M + 1)$ and V_{acc} is an accessible volume where the particles are created, Λ is the De Broglie wavelength and $\Delta E_{N_M+1,N_M}$ is the potential energy change due to the creation of an atom on the system.

Removal of an atom: a Pd atom is chosen at random and a removal attempt is accepted with probability:

$$W_{N_M\rightarrow N_M-1} = \min[1,\Gamma\exp(-\beta\{\mu + \Delta E_{N_M-1,N_M}\})]$$

where $\Gamma = \Lambda^3 N_M/V_{acc}$ and $\Delta E_{N_M-1,N_M}$ is the potential energy change due to the elimination of an atom on the system. This trial move mimics the dissolution process or even more, the equilibrium between species.

4. Results and discussion

Fig. 1 shows the UV-vis spectra of the Au NPs (seeds) before and after the addition of Pd(II) bath. The seed spectrum (black line) exhibits the characteristic surface plasmon resonance (SPR) band at around 510–520 nm, as expected for *ca.* 5 nm diameter Au NPs.[28] Upon the addition of Pd(II) bath, the resulting spectrum exhibits only a gradual increase in absorption toward the blue and a decreasing profile with a noticeably increased extinction, where the SPR band of the former seeds is barely noticeable near 520 nm. From this evidence, it may be inferred that a Pd shell has been formed and dominates the optical properties of the nanoparticles.[29] Such a result also suggests that the nucleation of Pd NPs is negligible; otherwise the resulting spectrum would retain the SPR peak of Au NPs among its main features. This finding constitutes an indirect corroboration that experimental conditions do contribute to the inhibition of nucleation of Pd NPs. However, this observation cannot help in distinguishing whether the attenuation of the Au resonance comes from either the formation of a Pd shell or an Au–Pd surface alloy, as both scenarios would have similar effects.[30]

The changes in the optical properties as a function of shell thickness have already been predicted. Hofmeister *et al.*[31] obtained the theoretical extinction spectra of Au@Pd core–shell nanoparticles of different sizes, based on the Mie-like model. Also, Park and co-workers modeled the extinction spectra of Au@Pd core–shell nanoparticles by using the discrete dipole approximation (DDA) method.[32] A qualitative agreement between experiment and theoretical trends has been observed for Au@Pd core–shell NPs.

The Au NP seeds were analyzed using high resolution electron microcopy prior to the addition of the Pd metastable bath. In Fig. 2, several TEM and STEM images are shown at different levels of magnification. At low magnification, the uniform size distribution of the Au seeds (6 ± 1 nm) can be observed, whereas at high magnification, a detailed inspection of single seeds reveals high-index planes on the surface of the NPs (see Fig. 2c).

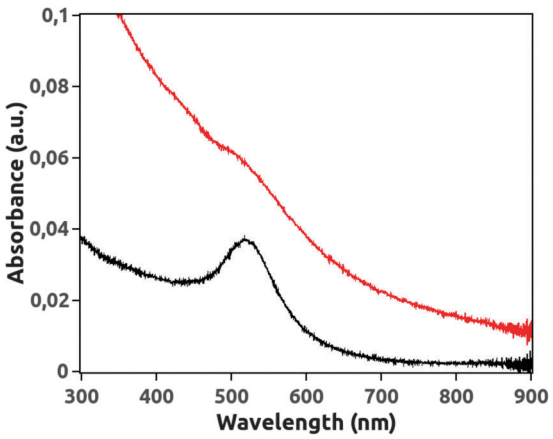

Fig. 1 UV-vis spectra of Au seeds before (black line) and after (red line) the addition of Pd(II) bath.

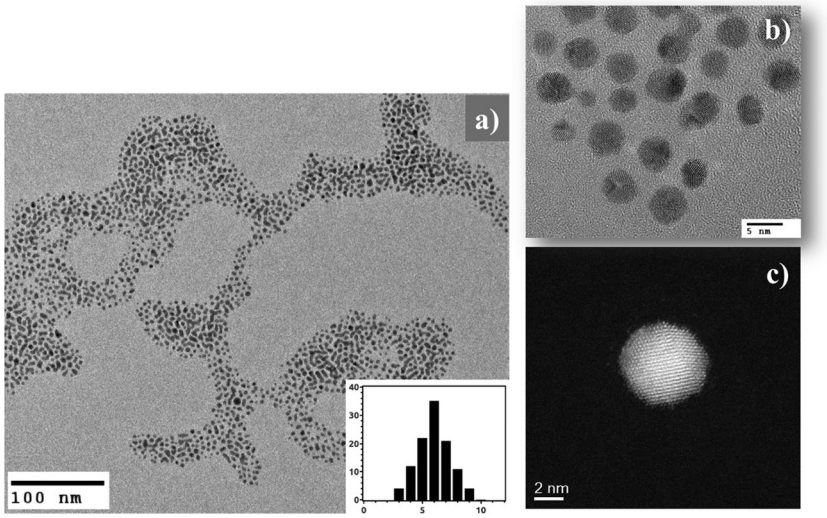

Fig. 2 (a) Low magnification TEM image of Au NP seeds (inset: size distribution histogram), (b) high-magnification TEM image and (c) high resolution STEM image taken at 80 kV.

Fig. 3(a) displays a representative HAADF-STEM image of the sample, five minutes after the last addition of Pd(II) bath, confirming the presence of Au@Pd core–shell nanoparticles. The STEM image shows a clear contrast difference between the core's gold atoms and palladium atoms at the shell due to their different atomic density values. Since the intensity signal depends strongly on the atomic number (Z), the Pd shell appears less intense than the Au core. The calculated diameter of the core of the Au@Pd particles is 6.7 ± 0.1 nm, giving an average shell thickness of 1.3 ± 0.8 nm. This value is consistent with the calculated shell thickness (1.39 nm) using the following equation:[33]

$$D_{\text{core-shell}} = D_{\text{core}}\left(1 + \frac{V_{\text{Pd}}[\text{Pd}]}{V_{\text{Au}}[\text{Au}]}\right)^{1/3}$$

where D_{core} is the diameter of the experimentally measured Au core (6 nm), and V_{Pd} and V_{Au}, and [Pd] and [Au] are the molar volumes and concentrations of Pd and Au, respectively.

The distribution of Au and Pd was studied by energy dispersive X-ray spectroscopy (EDS). Fig. 3(b) shows the EDS line profile of Au and Pd, measured through the center of an individual nanoparticle (marked by a green line in Fig. 3(b)). Both the Au and the Pd signals were clearly traced across the entire particle, but the EDS spectrum indicates that the surface region is enriched with Pd atoms while the core is mainly constituted by Au. It can also be noted how the spheroidal shape of the core seeds is captured by the EDS line profile, in which a higher intensity signal is obtained at the center of the NPs.

It can be stated at this point that the present synthesis route allows us to obtain multilayer Au(core)–Pd(shell) nanoalloys in all cases. However, as described above, most of the theoretical calculations predict Pd(core)–Au(shell) structures when considering only 1 ML. Nevertheless, there is a very recent report[34] in which the effect of multilayers was analyzed. In that work the authors suggest that for large size and multiple ML, the Au(core)–Pd(shell) structures could be energetically more stable than the Pd(core)–Au(shell) ones.

In order to consider different scenarios, the energetic stability of several core–shell structures has been computed using embedded atom potentials and was analyzed by means of the excess energy (Δ) parameter defined as:

$$\Delta = \frac{E_{\text{NP}} - n_{\text{Pd}}E_{\text{Pd}}^{\text{bulk}} - n_{\text{Au}}E_{\text{Au}}^{\text{bulk}}}{(n_{\text{Pd}} + n_{\text{Au}})^{2/3}}$$

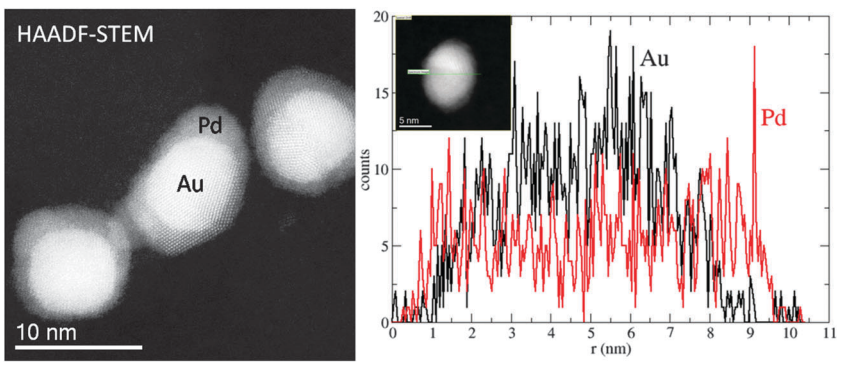

Fig. 3 (a) HAADF-STEM image of Au(core)–Pd(shell) nanoalloys. (b) EDS profile line of a selected nanoparticle.

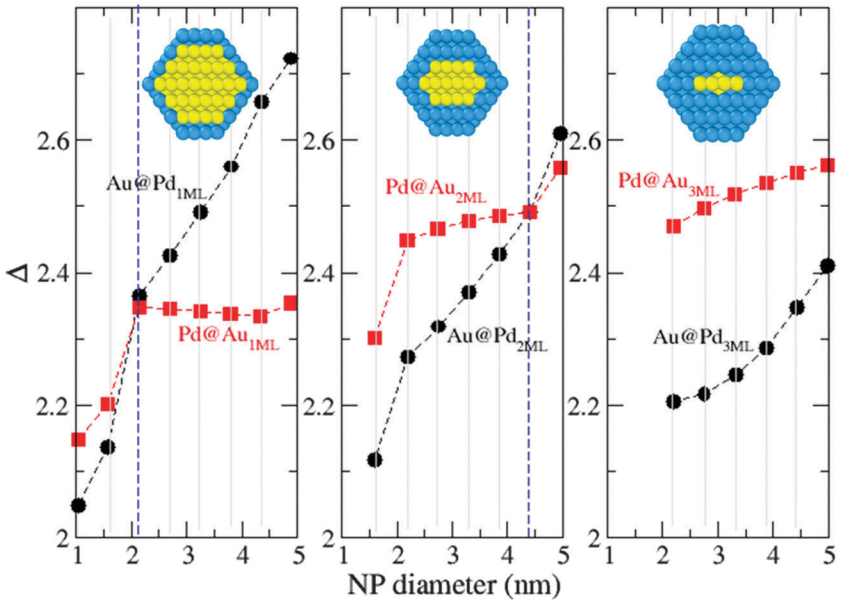

Fig. 4 Excess energy as a function of NP size for core–shell structures with different shell-thicknesses (1 ML, 2 ML and 3 ML) in the case of C_O geometry.

where E_{NP} is the total energy of the core–shell NPs; E_{Pd}^{bulk} and E_{Au}^{bulk} are the cohesive energies of Pd and Au, respectively; and n_{Pd} and n_{Au} are the number of Pd and Au atoms in the NPs, respectively. The more stable a morphological configuration becomes, the lower the value of Δ parameter.[35]

Several calculations were performed using different NP shapes, *i.e.* single crystal fcc-cuboctahedra (C_O), multiple-twinned icosahedra (I_h) and Marks decahedra (D_h). Also the core size and shell thickness were varied in order to analyze the variation of stability. In Fig. 4, excess energy (Δ) as a function of NP diameter is shown for NPs protected by different numbers of shells or monolayers (ML). In the case of NPs covered by only one ML the Au@Pd system is more stable for NPs with size smaller than 2 nm in diameter, whereas for larger sizes, Pd@Au core–shell structures are thermodynamically preferred. Interestingly, as the number of shells protecting the core increases, the crossover occurs at larger sizes. For instance, for two ML it occurs at sizes near 4.5 nm in diameter and for three ML it is expected at *ca.* 6.5 nm by interpolation.

This curious behavior has been observed for all nanoparticle shapes and is shown in Fig. S3 and S4 in the ESI.†

Full atomistic simulations using two different sampling algorithms were performed with the aim of understanding the growth mechanism of Au@Pd core–shell NPs with different core shapes. In this sense, we have chosen D_h and truncated octahedral (fcc-T_O) geometries because both NP morphologies are commonly observed in experimental STEM micrographs.

In Fig. 5, selected snapshots taken during different simulation stages are shown for (D_h) gold cores. In frames (a–c) the results of gcMC are presented, whereas in frames (d–f) the gcLD ones are shown. As observed by inspection of the atomic configurations, at early stages of the deposition process, Pd atoms starts to nucleate on the (111) faces, close to the edges, a phenomenon observed using both sampling algorithms.

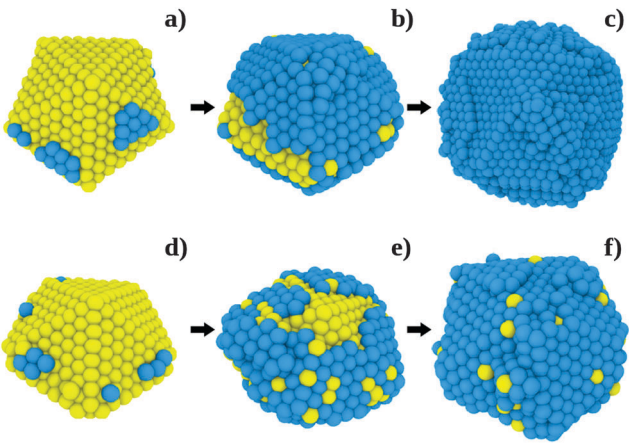

Fig. 5 Snapshots taken during evolution of Pd (blue) deposition on the Au (yellow) decahedron at T = 300 K, μ = 1 eV: gcMC (upper panel) and gcLD (lower panel). Solution atoms are not shown for simplicity. (a) and (d) $Au_{95}Pd_5$. (b) and (e) $Au_{65}Pd_{35}$. (c) $Au_{15}Pd_{85}$. (f) $Au_{45}Pd_{55}$.

As the number of Pd atoms increases, the second Pd layer starts to grow before the first ML is completed, *i.e.* a layer-by-layer growth mechanism is never observed. However it should be noted that the gcLD sampling algorithm shows some degree of surface alloys, even at an intermediate stage, *i.e.* before the gold seed is completely covered by palladium. The nature of the intrinsic dynamics, which is capable of reproducing concerted diffusion mechanisms, may possibly be responsible for the observed discrepancy between Metropolis Monte Carlo and Langevin dynamics results.

As mentioned above, the same kind of simulation was performed for other core shapes. For instance, in Fig. 6 the gcMC and gcLD results obtained for Pd growth on gold cores with truncated octahedral shape are shown. In this case the results are somewhat different. At early stages of Pd atom

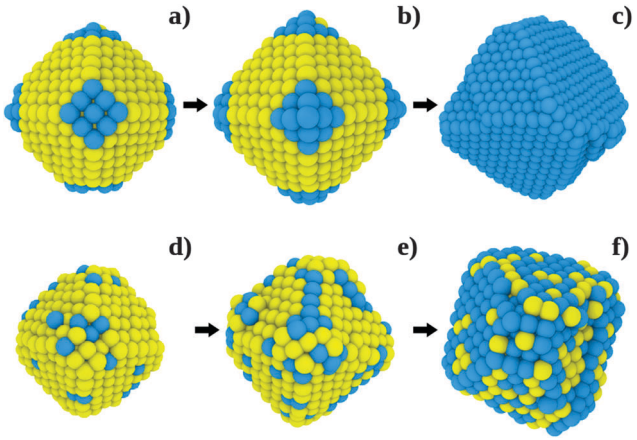

Fig. 6 Snapshots taken during evolution of Pd (blue) deposition on the Au (yellow) truncated octahedron at T = 300 K, μ = 1 eV: gcMC (upper panel) and gcLD (lower panel). Solution atoms are not shown for simplicity. (a) and (d) $Au_{95}Pd_5$. (b) and (e) $Au_{85}Pd_{15}$. (c) $Au_{30}Pd_{70}$. (f) $Au_{60}Pd_{40}$.

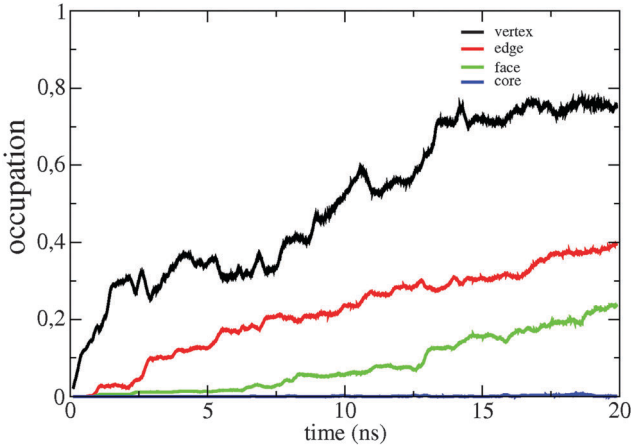

Fig. 7 Relative Pd occupation of each site of the decahedron.

deposition, the (100) facets seem to be preferred in both simulation techniques. However, in the case of gcLD, some degree of mixing between Au and Pd is evident, in agreement with the results presented before for D_h structures. Again, the second Pd layer starts to grow before the first Pd ML is completed. The final structures obtained with both methods are different in this case, whereas in the case of gcMC a core–shell structure is observed, the gcLD shows a core–shell structure with mixing of elements at the surface (see a cross-section of this structure in Fig. S5 – ESI†). The latter structure has been observed experimentally by many other authors.[13,36] It can be summarized at this point that the atomistic simulations are an important tool to predict structures, which can be directly correlated with those observed in the experiments (see an EDS profile comparison between simulation and experiment in Fig. S10 – ESI†). But, it cannot be forgotten that in conventional experiments, NPs are not likely to be restricted to vacuum. Conversely, NPs are generally exposed to solvents, and this causes friction. In such cases sporadic high velocity collisions will perturb the system, and can generate different structures and evolutionary phenomena. In this sense the gcLD results should be more realistic than molecular dynamics or Monte Carlo simulations.

With the purpose of quantifying in more detail how the deposition of Pd atoms proceeds through different atomic sites, we computed the occupation number as a function of time. The different sites are determined by the coordination number of each atom. The internal atoms are bonded to 10 or more atoms. The coordination number between 9 and 6 corresponds to facets, while the coordination numbers of 5 and 4 are matched to edge sites. Lower coordination numbers are consistent with vertex atoms. In Fig. 7, the relative occupation of each site (*i.e.* vertex, edges, facets and internal-core) is plotted against simulation time for the case of D_h gold seeds. As observed, the vertex atoms are initially occupied, followed by edges and facets. In the case of T_O gold seeds (Fig. 8), vertex and edge sites are occupied firstly, and facets and internal core sites subsequently. This information gives a clear picture of how the growth mechanism evolves towards the final core–shell structures observed experimentally.

The atomic configurations shown in Fig. 5c, 5f, 6c and 6f (obtained with gcMC and gcLD respectively) were used as input to simulate HAADF-STEM images. For these simulations we used the multislice method as implemented in the *xHREM* package,[37] by Ishizuka[38] that uses an algorithm based on Fast Fourier Transformation. In the simulated HAADF-STEM, the particle acting as a sample was dissected into 20 slices (in the direction of the electron beam), each slice treated independently through an averaged projected potential. In accordance with the experimental STEM images used in this study, the simulated microscope was set at an electron beam voltage of 200 kV, with a resolution close to 0.1 nm. The simulated micrographs and the experimental STEM images are presented in Fig. 9. Remarkably, all the simulated micrographs resemble those obtained experimentally, and a direct comparison between experimental images and atomistic simulation results can be done. In both cases, the regions enriched in Au appear brighter than the regions rich in Pd, since the intensity signal depends strongly on the atomic number (Z). The core–shell structure is clearly visible in the structures of the upper panel,

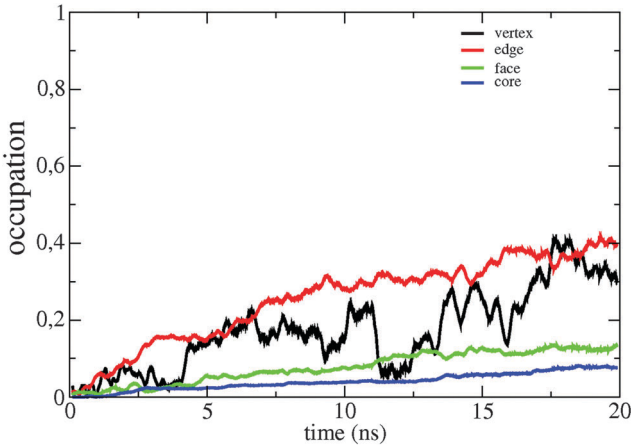

Fig. 8 Relative Pd occupation of each site of the truncated octahedron.

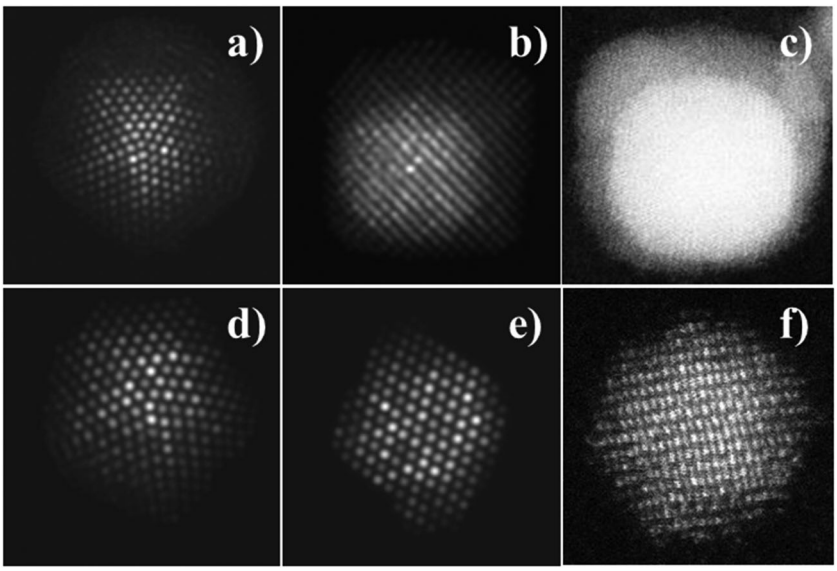

Fig. 9 Simulated HAADF-STEM images of Au(core)–Pd(shell) bimetallic nanoparticles. (a) and (b) D_h structure taken from gcMC and gcLD simulations respectively; (d) and (e) fcc-T_O structure taken from gcMC and gcLD simulations respectively. (c) and (f) experimental STEM images of the sample.

while in the bottom one the mixing of the two species on the surface is more noticeable. It is important to highlight how the simulations qualitatively reproduce the experimental results, providing, at the same time, valuable insight into the growth mechanism. In addition, Fig. S6–S9, ESI,† show that the structures were rotated 0°, 45° and 90° on *y*- and *x*-axes.

5. Conclusions

In summary, gold–palladium core–shell nanoalloys have been produced through a facile synthesis method, where pre-synthesized gold seeds were covered by a few Pd monolayers. It should be stressed that the synthesis route does not use any surfactant or protective organic molecule to prevent coalescence. Aberration corrected HAADF-STEM, in combination with high resolution spectral and chemical analysis, has allowed us to study the atomic structure of Au@Pd nanoalloys in atomic detail.

Using embedded atom calculations, we were able to establish how the chemical order of the core–shell structure of Au@Pd and Pd@Au could lead to stable configurations, and how the number of Pd or Au ML could affect that stability. In general terms, a crossover between these kinds of core–shell structures depends on the nanoparticle size.

By using gcMC and gcLD, we have been capable of studying the nucleation and growth mechanism of Pd atoms on Au seeds with different shapes. The morphologies obtained with these simulations resemble very well with those obtained experimentally.

Acknowledgements

This work was financially supported by CONICET PIP 11220110100992, Universidad Nacional de Córdoba, ANPCyT Program BID (PICT 2010-1233). The authors acknowledge the Texas Advanced Computing Center (TACC) and the Sistema Nacional de Computación de Alto Desempeño (SNCAD). The group of UTSA wish to thank the National Center for Research Resources (5 G12RR013646-12) and the National Institute on Minority Health and Health Disparities (G12MD007591) of the National Institutes of Health. The authors would like to acknowledge the NSF for support with grants DMR-1103730, ''Alloys at the Nanoscale: The Case of Nanoparticles Second Phase and PREM: NSF PREM Grant # DMR 0934218; ''Oxide and Metal Nanoparticles – The Interface Between Life Sciences and Physical Sciences''. In addition, the authors would like to acknowledge the support of the Welch Foundation (grant No. AX-1615, ''Controlling the Shape and Particles Using Wet Chemistry Methods: The Case of Bimetallic Nanoparticles'').

References

1 R. Wang, O. Dmitrieva, M. Farle, G. Dumpich, M. Acet, S. Mejia-Rosales, E. Perez-Tijerina, M. J. Yacaman and C. Kisielowski, *J. Phys. Chem. C*, 2009, **113**, 4395–4400.
2 H. L. Liu, C. H. Sonn, J. H. Wu, K.-M. Lee and Y. K. Kim, *Biomaterials*, 2008, **29**, 4003.
3 R. Ferrando, J. Jellinek and R. L. Johnston, *Chem. Rev.*, 2008, **108**, 845.
4 H. Zhang, T. Watanabe, M. Okumura, M. Haruta and N. Toshima, *Nat. Mater.*, 2012, **11**, 49–52.
5 J. Xu, T. White, P. Li, C. He, J. Yu, W. Yuan and Y.-F. Han, *J. Am. Chem. Soc.*, 2010, **132**, 10398.
6 E. Gross, I. Popov and M. Asscher, *J. Phys. Chem. C*, 2009, **113**, 18341.
7 N. El Kolli, L. Delannoy and C. Louis, *J. Catal.*, 2013, **297**, 79–92.
8 L. Zhang, A. Wang, J. T. Miller, X. Liu, X. Yang, W. Wang, L. Li, Y. Huang, C.-Y. Mou and T. Zhang, *ACS Catal.*, 2014, **4**(5), 1546–1553.

9 R. W. J. Scott, O. M. Wilson, S. K. Oh, E. A. Kenik and R. M. Crooks, *J. Am. Chem. Soc.*, 2004, **126**, 15583–15591.
10 M. S. Chen, D. Kumar, C. W. Yi and D. W. Goodman, *Science*, 2005, **310**, 291–293.
11 D. I. Enache, J. K. Edwards, P. Landon, B. Solsona-Espriu, A. F. Carley, A. A. Herzing, M. Watanabe, C. J. Kiely, D. W. Knight and G. J. Hutchings, *Science*, 2006, **311**, 362–365.
12 A. Gopalan, D. Ragupathy, H.-T. Kim, K. M. Manesh and K.-P. Lee, *Spectrochim. Acta, Part A*, 2009, **74**, 678–684.
13 M. G. Weir, M. R. Knecht, A. I. Frenkel and R. M. Crooks, *Langmuir*, 2010, **26**(2), 1137–1146.
14 M. M. Mariscal, A. Mayoral, J. A. Olmos-Asar, C. Magen, S. Mejía-Rosales, E. Pérez-Tijerina and M. J. Yacamán, *Nanoscale*, 2011, **3**, 5013.
15 A. J. Logsdai and R. L. Johnston, *RSC Adv.*, 2012, **2**, 5863–5869.
16 Y. W. Lee, M. Kim, Y. Kim, S. W. Kang, J.-H. Lee and S. W. Han, *J. Phys. Chem. C*, 2010, **114**, 7689–7693.
17 D. Ferrer, A. Torres-Castro, X. Gao, S. Sepúlveda-Guzmán, U. Ortiz-Méndez and M. J. Yacamán, *Nano Lett.*, 2007, **7**, 1701–1705.
18 C. Li, W. Cai, C. Kan and G. Fu, *Scr. Mater.*, 2004, **50**, 1481.
19 M. O. Nutt, J. B. Hughes and M. S. Wong, *Environ. Sci. Technol.*, 2005, **39**, 1346.
20 R. Ismail and R. L. Johnston, *Phys. Chem. Chem. Phys.*, 2010, **12**, 8607–8619.
21 F. Pittaway, L. O. Paz-Borbón, R. L. Johnston, H. Arslan, R. Ferrando, C. Mottet, G. Barcaro and A. Fortunelli, *J. Phys. Chem. C*, 2009, **113**, 9141.
22 I. V. Yudanov and K. M. Neyman, *Phys. Chem. Chem. Phys.*, 2010, **12**, 5094–5100.
23 O. A. Oviedo, L. Reinaudi, M. M. Mariscal and E. P. M. Leiva, *Electrochim. Acta*, 2012, **76**, 424–429.
24 M. Mariscal, E. P. M. Leiva, K. Pötting and W. Schmickler, *Appl. Phys. A: Mater. Sci. Process.*, 2007, **87**, 385–389.
25 W. Schmickler, K. Pötting and M. Mariscal, *Chem. Phys.*, 2006, **320**, 149–154.
26 P. Allen and D. J. Tildesley, *Computer Simulation of Liquids*, Clarendon, 1987.
27 X. Zhou, R. Johnson and H. Wadley, *Phys. Rev. B: Condens. Matter Mater. Phys.*, 2004, **69**, 144113.
28 T. Shimizu, T. Teranishi, S. Hasegawa and M. Miyake, *J. Phys. Chem. B*, 2003, **107**, 2719–2724.
29 A. Henglein, *J. Phys. Chem. B*, 2000, **104**, 6683.
30 M. B. Cortie and A. M. McDonagh, *Chem. Rev.*, 2011, **111**, 3713–3735.
31 C. Kan, W. Cai, C. Li, L. Zhangand and H. Hofmeister, *J. Phys. D: Appl. Phys.*, 2003, **36**, 1609–1614.
32 D. Y. Kim, K. W. Choi, X.-L. Zhong, Z.-Y. Li, S. H. Im and O. O. Park, *CrystEngComm*, 2013, **15**, 3385.
33 J. H. Hodak, A. Henglein, M. Giersig and G. V. Hartland, *J. Phys. Chem. B*, 2000, **104**, 11708–11718.
34 A. J. Logsdail and R. L. Johnston, *RSC Adv.*, 2012, **2**, 5863–5869.
35 F. Baletto, in *Metal Clusters and Nanoalloys. Nanostructure Science and Technology Series*, ed. M. M. Mariscal, *et al.*, Springer, 2013, ch. 8, 243–273.
36 S. W. T. Price, J. M. Rhodes, L. Calvillo and A. E. Russell, *J. Phys. Chem. C*, 2013, **117**, 24858–24865.
37 http://www.hremresearch.com/.
38 K. Ishizuka, Proc. International Symposium on Hybrid Analyses, 1998, 69–72.